IOP Publishing Smart Materials and Structures
Smart Mater. Struct. **34** (2025) 035021 (14pp) https://doi.org/10.1088/1361-665X/adb4b3

Printed ultrasound sensors for enhanced structural health monitoring: development, characterization, and real-time evaluation

Eliott Brun[1], Elsa Dos Santos[1,4], Guilhem Rival[1], Pierre-Jean Cottinet[1], Arnaud Pelletier[2] and Benjamin Ducharne[1,3,*]

[1] LGEF, INSA-Lyon, UR682, University Lyon, 69621 Villeurbanne, France
[2] CMPhy, 26 Rue Paul Sabatier, 71530 Crissey, France
[3] ELyTMaX IRL3757, CNRS, Univ Lyon, INSA Lyon, Centrale Lyon, Université Claude Bernard Lyon 1, Tohoku University, Sendai, Japan
[4] Arc en Ciel Sérigraphie, ZI LE Forestier, 42630 Regny, France

E-mail: benjamin.ducharne@insa-lyon.fr

Received 14 December 2024, revised 27 January 2025
Accepted for publication 11 February 2025
Published 19 February 2025

Abstract

This study presents the development of ultrasound (US) sensors for structural health monitoring (SHM) by directly printing the sensors onto structural components. Unlike traditional ultrasound-based SHM systems, this approach minimizes sensor placement and environmental interference challenges, providing a stable, durable, and cost-effective solution for long-term monitoring of critical infrastructure. The core of this technology is a piezoelectric composite made of an OE 132–43/P189 mixture at 80 vol.% ferroelectric particles in a polyimide matrix, selected for its optimal dielectric strength, consistent d_{33} polarization, high-frequency response (1–20 MHz), and high thermal stability. Experimental validation showed that the printed sensors effectively measured component thickness in steel and aluminum, confirming their suitability for non-destructive evaluation. Additionally, multi-layer sensor designs were explored, producing higher acoustic pressure at lower operating voltages, enabling applications on thicker materials. This work advances SHM by enabling continuous, real-time monitoring, improving structural safety, and reducing maintenance costs across various industries.

Keywords: piezoelectric composite, dielectric strength, dielectric spectroscopy, non-destructive evaluation, thickness evaluation

1. Introduction

Structural health monitoring (SHM) is vital for ensuring the safety and longevity of critical infrastructure, such as bridges, buildings, and pipelines [1, 2]. By continuously assessing structural integrity, SHM helps detect early signs of wear or damage, enabling timely maintenance and preventing catastrophic failures. This proactive approach enhances public safety, reduces repair costs, and extends the lifespan of structures. In industries like aerospace and energy, SHM is particularly valuable for optimizing performance and minimizing downtime through real-time insights into structural behavior under varying conditions [3, 4].

SHM employs various non-destructive techniques (NDT) to evaluate structures without causing damage. Visual inspections, while common, are limited to surface-level insights

* Author to whom any correspondence should be addressed.

© 2025 IOP Publishing Ltd. All rights, including for text and data mining, AI training, and similar technologies, are reserved.

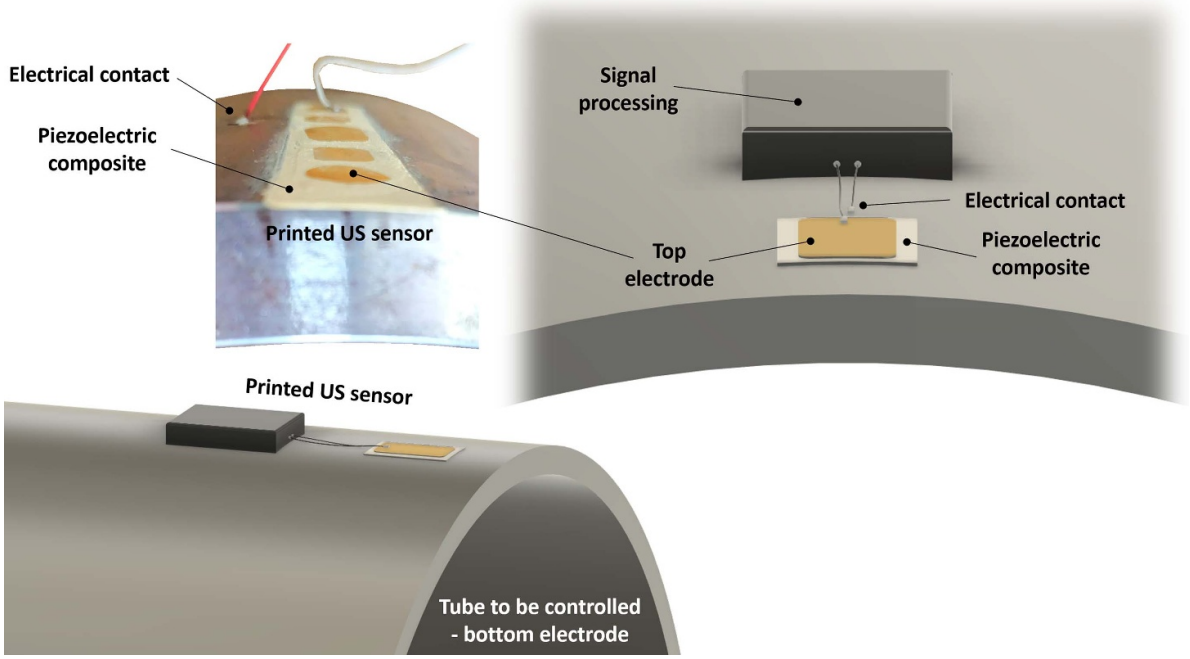

Figure 1. Illustration of a printed ultrasound sensor.

[5]. Vibration-based methods detect damage through changes in structural dynamics, such as frequency shifts [6, 7]. Electromagnetic techniques, such as eddy current testing, identify surface defects in conductive materials [8, 9], while thermal imaging reveals hidden flaws through heat distribution patterns. Ultrasound stands out as an especially versatile technique, enabling the detection of internal defects like cracks and voids by analyzing the behavior of high-frequency sound waves [10]. Changes in wave speed, amplitude, or direction indicate material degradation or damage, such as corrosion or fatigue cracks, that might not be visible externally.

Despite its versatility, ultrasound-based SHM faces challenges, particularly in sensor reproducibility [10, 11]. Measurements are highly sensitive to sensor positioning and coupling pressure, making results prone to inconsistency. Environmental factors like temperature and surface conditions further affect sensor performance, leading to potential false readings or difficulties in reproducing results [12].

Several solutions exist to address these challenges. Automated or permanently mounted sensors ensure consistent placement and contact pressure [13]. Sensor arrays or phased arrays improve coverage and reduce misalignment issues [14, 15]. Advanced signal processing techniques, such as baseline subtraction, help mitigate environmental effects [16]. Regular sensor calibration and consistent surface preparation can further enhance reliability.

While effective, these solutions involve complexities, such as installation challenges, ongoing calibration, and susceptibility to environmental interference [17, 18]. This study proposes an alternative to overcome these limitations: printing sensors directly onto the monitored structure (see figure 1). This approach integrates sensor placement during manufacturing, eliminating manual positioning issues and allowing continuous monitoring without operational disruptions. Additionally, printed sensors ensure a stable interface with the structure, reducing maintenance needs and providing reliable long-term data [9, 19–21].

By optimizing materials and printing techniques, we achieved highly functional, durable sensors capable of continuous monitoring without additional installation steps. This approach maintains the integrity of critical parts and makes it economically feasible to monitor larger surfaces, reducing costs compared to traditional sensor deployment methods.

2. Ultrasound printed sensors

2.1. Structure of an ultrasound printed sensor

In NDT for SHM, ultrasound sensors often require miniaturization to meet space constraints or allow integration on thin surfaces. This feature is typically achieved using piezoelectric composite films, which consist of a polymer matrix mixed with micrometer-sized ferroelectric particles [22, 23]. Once polarized, these films exhibit piezoelectric properties, making them suitable as sensing elements [24].

The structure of a piezoelectric composite sensor is straightforward: a piezoelectric composite layer is sandwiched between two electrodes (figure 2(a)). For conductive substrates, the substrate itself can serve as the bottom electrode, provided it has a smooth and defect-free surface (figure 2(b)). However, surface imperfections can compromise electrical contact and reduce sensor performance.

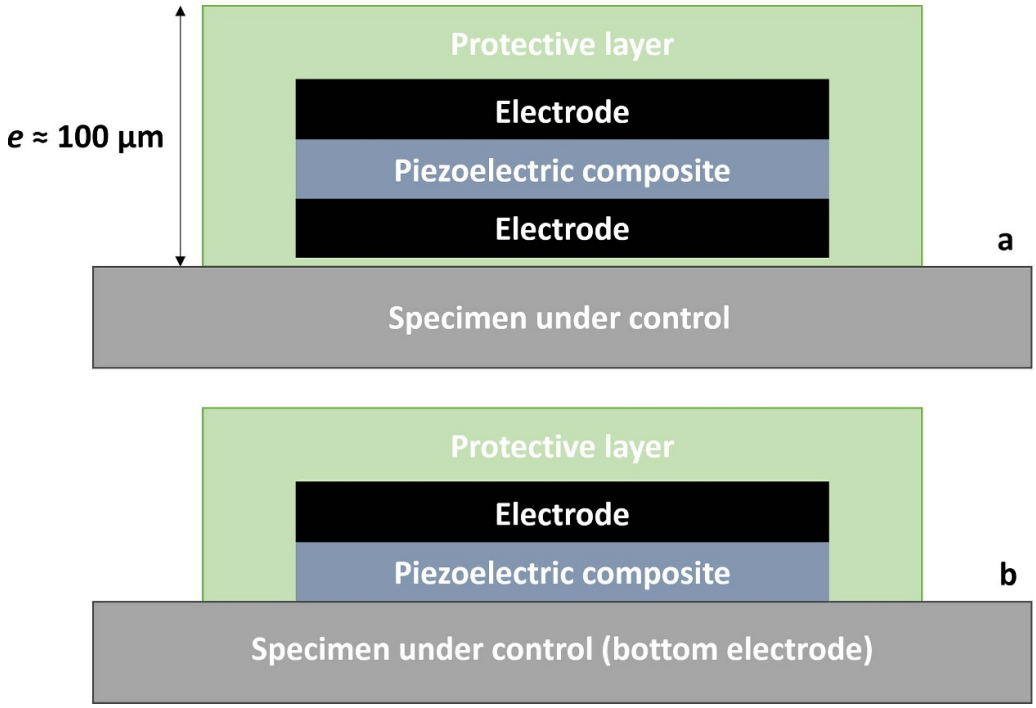

Figure 2. Typical structure of a SHM ultrasound sensor (a) layered configuration, (b) the specimen under control is electrically conductive and plays the role of the bottom electrode).

Notably, the piezoelectric vibratory effect is amplified when the excitation frequency matches the composite's mechanical resonance frequency, which depends on the layer's thickness [25, 26]. Adjusting this thickness allows sensors to operate at specific test frequencies tailored for materials like metals or fiber composites [27]. This tuning enhances sensitivity, resolution, and performance for various applications.

The resonant frequency of the sensor (f_0) in equation (1) can be calibrated to align with the natural resonance of the tested material, maximizing the piezoelectric response.

$$f_0 = \frac{v}{2e} \tag{1}$$

$$v = \sqrt{\frac{C_{33}}{\rho}} \tag{2}$$

Where e is the piezoelectric patch thickness, v is the speed of sound (or acoustic wave velocity) in the piezoelectric material in the direction of thickness, C_{33} is the elastic modulus for thickness mode, and ρ is the density.

Piezoelectric composites have lower piezoelectric coefficients than solid ceramics, with d_{33} values typically lower by 10–100 pC·N^{-1} (table 2 in [28]). They necessitate higher electric fields to achieve the same vibratory effect, posing challenges for thick composites. As the thickness increases, so does the required voltage. For instance, generating an electric field of 10 V·μm^{-1} for ultrasonic actuation in composites thicker than 1 mm could demand voltages exceeding 1 kV, which is impractical for standard NDT devices limited to 500 V [22, 29].

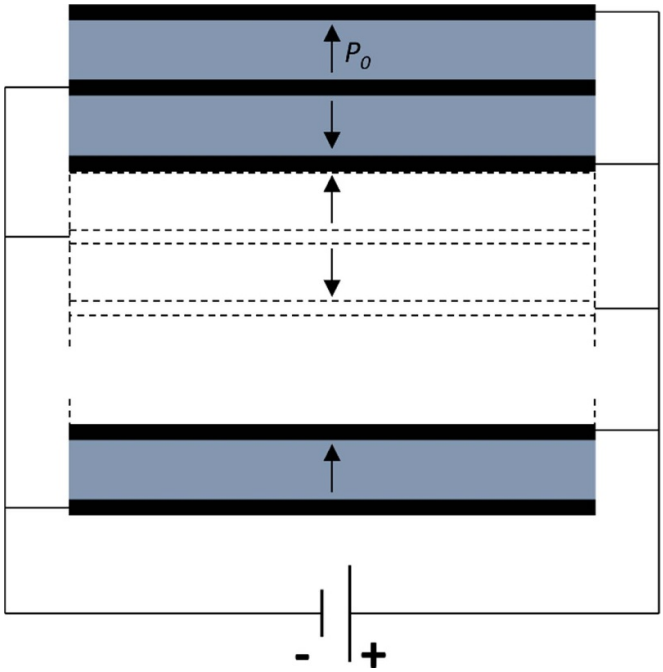

Figure 3. Typical structure of a SHM ultrasound multi-layer transducer (where P_0 gives the polarization direction).

A promising solution is using multi-layer transducers (figure 3). By stacking multiple piezoelectric layers with alternating electrodes, the same resonant frequencies as a single thick layer can be achieved while significantly reducing the supply voltage requirements. This configuration increases the electric field for a given

voltage, enhancing compatibility with conventional NDT equipment [30, 31].

2.2. Piezoelectric composite

2.2.1. Piezoelectrical particles: description. Two commonly used piezoelectric materials for ultrasonic testing applications are barium titanate ($BaTiO_3$) and lead zirconate titanate (PZT) [32, 33].

This study imposes an additional constraint of temperature resistance, as the sensor must operate continuously at temperatures up to 200 °C, a requirement for nuclear-type applications [34]. While $BaTiO_3$, with its 120 °C Curie temperature, is unsuitable for such conditions, PZT offers a higher Curie temperature and ensures reliable performance.

PZT, with the chemical formula $PbZr_xTi_{1-x}O_3$ ($0 \leqslant x \leqslant 1$), is a ceramic material with a perovskite-type crystalline structure and strong ferroelectric properties [32, 34]. Its Curie temperature, ranging from 230 °C to 500 °C, can be tailored through doping.

PZT's lead content places it under the SGH08 hazard category (sensitizing, mutagenic, carcinogenic, and reprotoxic) [35], leading to regulatory restrictions that limit its availability and detailed material characterization. Despite these challenges, PZT remains a viable choice for this study due to its superior thermal stability and industrial applicability.

The ultrasonic sensors of this study use a pulse-echo configuration, where a single active element alternately transmits and receives signals [36]. This dual-role configuration requires a careful selection of composite particles. Hard PZT ceramics, with low losses and high thermal stability, are ideal for energy-efficient transmission.

Due to the miniaturization requirements, the active element is designed as a composite rather than a solid ceramic. Unfortunately, composites require higher electric fields for polarization, increasing the risk of dielectric breakdown.

While lead-free materials like potassium sodium niobate (KNN) would have solved the lead content issue, they currently fall short in performance and stability for demanding applications. Also, most of them are not commercially available. Therefore, PZT P189, a NAVY III-type piezoelectric ceramic produced by Saint-Gobain (France) and available in our laboratory, was selected as the active material of the composites [25, 37]. P189 combines high thermal stability with efficient energy transfer, meeting the demanding requirements of this study. Table 1 summarizes its physical properties [38, 39].

2.2.2. Piezoelectrical particles: characterization

- Particle size

We analyzed particle size with the laser diffractometer Mastersizer 2000 from Malvern Panalytical (UK). The results (figure 4) revealed a bimodal particle size distribution, with two distinct peaks at 1.3 and 8.2·μm and a median particle size of 1.4·μm. The presence of smaller particles within the composite facilitates the occupation of void spaces left by the larger particles, leading to improved final composite performances.

Table 1. P189 Properties.

	Unit	Typical value
Density	10^3 kg·m^{-3}	7,65
Curie temperature	°C	320
Relative dielectric Permittivity ε_{33}	—	1150
Loss angle (Tan δ)	%	0,05
Piezoelectric coefficient d_{33}	10^{-12} m·V^{-1}	240

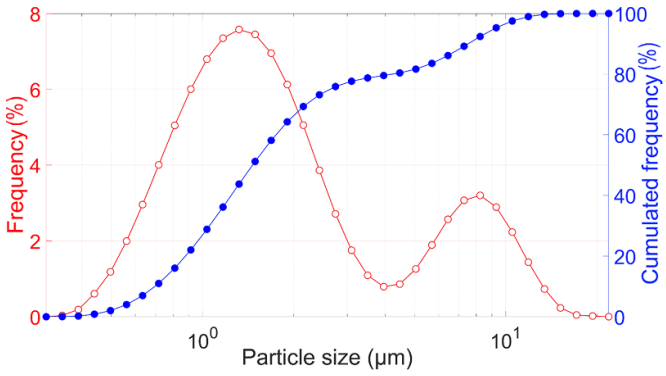

Figure 4. Particle size distribution.

- Curie temperature

A significant peak in permittivity marks the Curie temperature (T_c) of the P189 particles. As the temperature approaches T_c, thermal agitation disrupts the domain alignment, causing a rapid increase in dielectric permittivity. At T_c, the permittivity reaches its maximum. Beyond T_c, the material transitions from a ferroelectric to a paraelectric phase, decreasing permittivity. The Curie temperature can be precisely determined by monitoring this peak through capacitance measurements at 1 kHz during controlled heating of the piezoelectric material. Relative permittivity (ε_r)) can be calculated from equation (3).

$$\varepsilon_r = \frac{Cd}{A\varepsilon_0} \tag{3}$$

Where C is the capacitance measured, d is the sintered pellet thickness (1.85 mm), $A = \pi r^2$ is the pellet area with r = 6.625 mm and ε_0 the vacuum permittivity (8.85 10^{-12} F·m^{-1}).

Our measurements on P189 indicate a Curie temperature of 390 °C (figure 5), confirming its classification as an

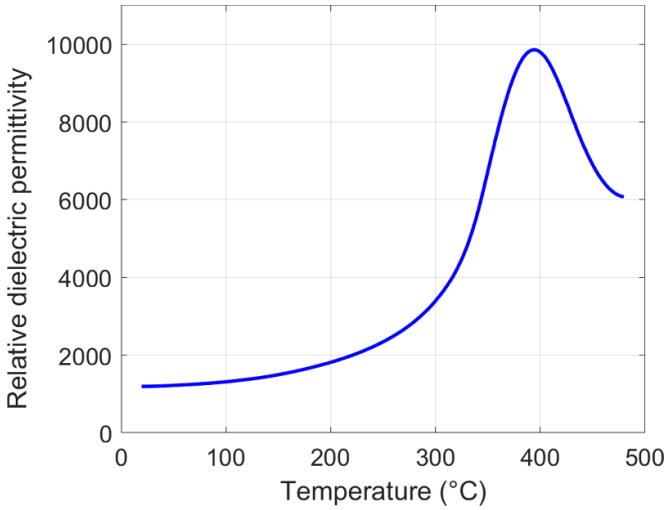

Figure 5. Relative permittivity thermogram of PZT P189 sintered pellets.

Table 2. Short list of the selected polymer matrix.

Manufacturer	Commercial reference	Nature
Finale Advanced materials (Paris, France)	Duralco 4460 Duralco 4461	Dielectric epoxy
Dupont (Wilmington, Delaware, USA)	HT 702	Dielectric polyimide
Epoxy technology Inc (Billerica, Massachusetts, USA)	OE 132–43	

intermediate-hard PZT suitable for the intended application. This high Curie temperature also substantiates P189's suitability for high-temperature applications.

2.2.3. Polymer matrix: description. The polymer matrix provides structural integrity and reduces system permittivity, optimizing electro-mechanical performance [40]. For ultrasonic transducers in NDT, the matrix must exhibit high rigidity to minimize energy losses from mechanical damping, ensuring effective acoustic energy transmission and improving sensitivity and accuracy.

The matrix must also maintain mechanical properties at elevated temperatures to ensure stability in industrial environments. High glass transition temperatures are essential to prevent thermal degradation, while high dielectric strength is needed to withstand the electric fields applied during polarization. Insufficient dielectric strength can lead to electrical breakdown, compromising the composite's integrity.

Considering these constraints, high-temperature epoxy and polyimide matrices were selected as suitable candidates. Four formulations (two epoxies and two polyimides) were evaluated for their performance under high-temperature, high-stress environments (table 2).

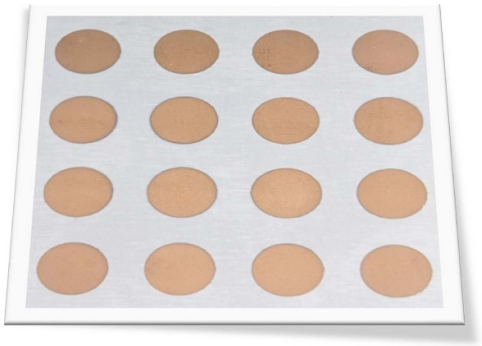

Figure 6. Picture of the tested polymer matrix discs.

It is worth mentioning that polyimides are generally known for their excellent thermal stability and resistance to environmental factors (humidity, etc.) [41, 42].

2.2.4. Polymer matrix: characterization

• Dielectric strength

The dielectric strength determines the polymer's capacity to withstand the high electric fields necessary for particle polarization. In this study, it was assessed through breakdown tests conducted on 16 discs, each with an 8 mm diameter (figure 6). A DC voltage was applied with a ramp rate of 500 $V{\cdot}s^{-1}$ until sample failure [43]. These tests were done at room temperature and resulted in a Weibull distribution (equation (4)), providing a cumulative statistical breakdown probability $P_i(E)$ for an applied electric field E.

$$P_i(E) = 1 - e^{-\left(\frac{E}{\eta}\right)^m} \tag{4}$$

With η is the critical breakdown electric field at which 63,2% of samples failed, and m a shape factor characterizing the distribution of sample's breakdown electric fields.

The breakdown probability also reflects the test-specific conditions, it is influenced by film thickness, electrode size, and temperature, which affect defect occurrence and free charge mobility, limiting conclusions about the general dielectric strength of the material.

Figure 7 displays the breakdown test results for table 2 polymer matrices, with experimental points and their associated Weibull distributions fitted with equation (4). Duralco 4460, HT702, and Epotek OE 132–43 matrices were tested under consistent conditions, including an average deposition thickness of 30·μm at room temperature. The Duralco 4461 matrix was excluded due to some inconsistency in the films thickness and poor substrate wettability, leading to deposit inhomogeneities.

For the three tested resins, the results demonstrate sufficient dielectric stiffness to support their use as matrices in the development of our targeted piezoelectric composites. The parameters corresponding to their Weibull distributions (equation (4)) are provided in table 3 below.

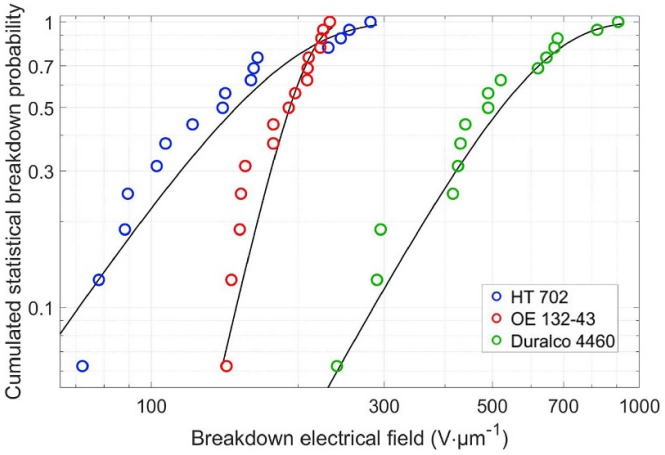

Figure 7. Weibull plot of the breakdown electric fields for the polymer matrices investigated.

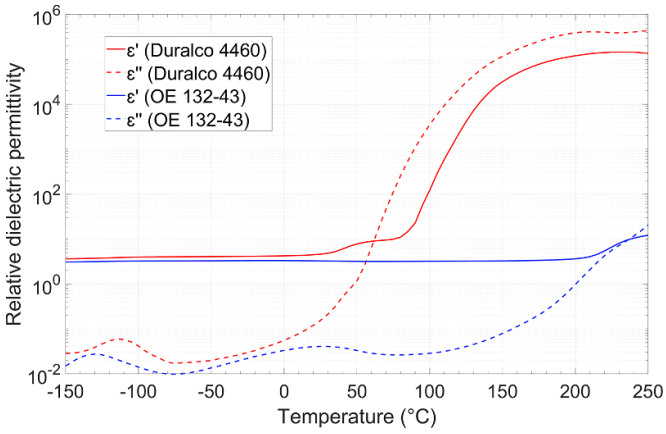

Figure 8. Conservative and dissipative permittivities thermograms of Duralco 4460 and OE 132–43.

Table 3. Weibull distribution (equation (4)) parameters for the three tested resins.

	Nature	η (V μm^{-1})	m
Duralco 4660	Epoxy	586	3,12
OE 132–43	Polyimide	201	7,45
HT 702	Polyimide	172	2,5

m reflects the distribution's spread and is associated with defects and inhomogeneities within the polymer matrix [44]. A comparison between the HT 702 and OE 132–43 matrices illustrates these influences: both are polyimide-based, with HT 702 containing silica particles and OE 132–43 comprising pure polyimide. The lower shape factor and broader distribution for HT 702 indicate a higher spread linked to extrinsic defects (i.e. silica particles). In contrast, the distribution for OE 132–43 is characteristic of polyimide's intrinsic properties. Similarly, the Duralco 4460 matrix shows indications of extrinsic failure, with observed degassing challenges suggesting a notable presence of defects, which accounts for these findings.

- Dielectric spectroscopy characterization

Dielectric spectroscopy was used to determine the optimal polarization temperature. At elevated temperatures, some polymers exhibit increased permittivity, enhancing polarization by concentrating the electric field in the lower-permittivity particle phase. However, higher temperatures also increase dielectric losses, raising the risk of dielectric breakdown. Thus, identifying an optimal polarization temperature is critical to balance effective polarization with breakdown risk.

In this study, dielectric spectroscopy was performed on Duralco 4460 and OE 132–43 matrices using a Novocontrol impedance analyzer (Germany) at 0.1 Hz with 5 °C increments. The HT 702 matrix was excluded due to its low dielectric breakdown strength. Results (figure 8) show that for Duralco 4460, the permittivity (ε') increases significantly from 90 °C, peaking at 250 °C, while losses (ε'') rise from 50 °C and peak at 200 °C. For OE 132–43, ε' remains stable up to 210 °C, with minimal losses until 200 °C. These findings suggest that at certain temperatures, the permittivities of the matrix and particles align, enhancing the polarization efficiency of the piezoelectric composite.

2.2.5. Substrate (bottom electrode). The substrate of the flat ultrasonic sensors developed in this study can be either a polymer film or a thin metallic sheet, depending on application requirements. Polymer substrates offer high flexibility [45]. For such cases, a conductive ink layer serves as the lower electrode.

Alternatively, thin metal sheets provide structural support and inherent electrical conductivity, simplifying manufacturing by removing the need for conductive ink. When the metal sheet is sufficiently thin (<200 μm), it retains flexibility comparable to polymer substrates, making it suitable for applications requiring some conformability.

High-temperature resistance further constrains polymer substrate selection. Polyimide film (125 μm thick Kapton) was chosen for its thermal stability and mechanical properties, ensuring reliability in high-temperature environments [46]. This material optimally balances flexibility and durability for ultrasonic sensor applications.

A critical challenge in using substrates is managing acoustic impedance mismatches, which can disrupt ultrasonic wave transmission and reduce sensor efficiency. Impedance matching, typically achieved through a quarter-wave plate (λ/4), minimizes this disruption by bridging impedance differences between the substrate and tested material [47]. The quarter-wave plate's thickness depends on the test frequency and the acoustic velocity (v_{mat}) in the substrate, as governed by equation (5):

$$\lambda = \frac{v_{mat}}{f}. \tag{5}$$

Designing the optimal substrate thickness ensures effective wave transmission and minimizes energy loss. Tailoring the substrate's properties, including thickness and material composition, is crucial for maximizing performance.

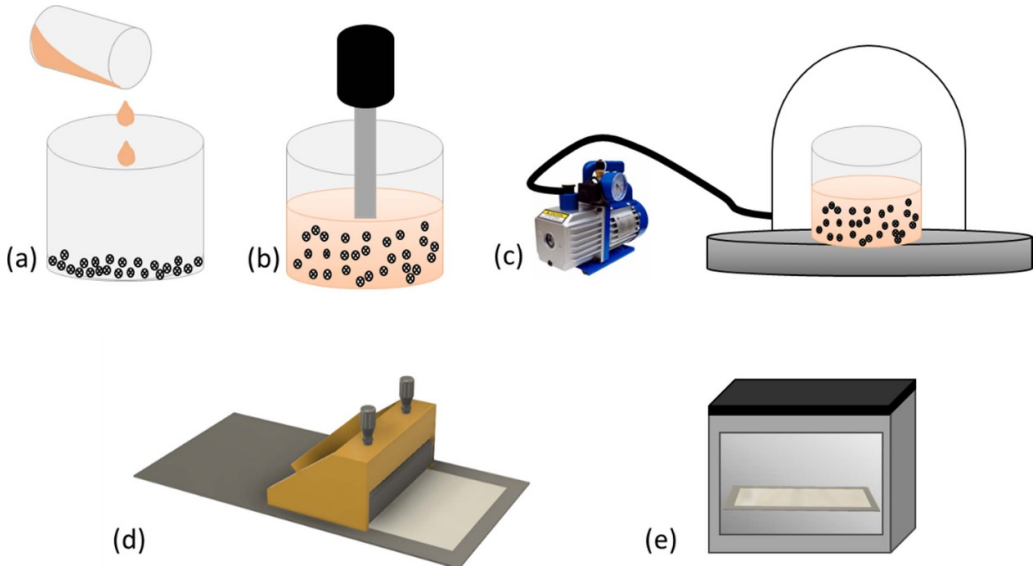

Figure 9. Piezoelectric composite film fabrication process. (a) Mixing stage. (b) Ultrasonic treatment. (c) Degassing stage. (d) Adjustable film deposit. (e) Oven stage.

For conductive test specimens, the piezoelectric layer can be applied directly to the part's surface, eliminating the substrate. This configuration avoids impedance mismatches, enhancing acoustic energy transfer and sensor performance. Such direct application is particularly advantageous in high-precision applications requiring minimal signal attenuation.

2.2.6. Top electrode. In initial tests, the upper electrode can be applied by physical sputtering, but this method is unsuitable for industrial US sensors due to rapid gold degradation. For durability, conductive ink is required, using either silver paint or a paste of silver particles in a polymer. The choice depends on adhesion and high-temperature durability.

Electrode deposition demands a smooth piezoelectric composite surface. However, ink deposition may create microscopic open porosities, allowing solvent infiltration that reduces breakdown voltage. Steps to improve surface quality include degassing the mixture, screen printing, and resting the deposit at 80 °C to fluidify the ink and fill voids.

2.3. Manufacturing process

2.3.1. Initial mixture. The preparation of the piezoelectric composite involved precise mixing of piezoelectric powder and polymer matrix. The powder was finely ground with an agate mortar to minimize aggregates and weighed precisely. The polymer, including resin and hardener (for epoxy), was added in pre-calculated amounts for the desired matrix-to-particle ratio, accounting for solvent evaporation. After initial manual mixing, the blend underwent ultrasonic treatment using a UP400S ultrasound device (Hielscher Ultrasonics, Germany) to disperse particles. The composite was further processed in a speed mixer to eliminate the remaining clusters. Finally, the mixture was degassed in a vacuum chamber to remove air and voids, ensuring uniformity and high performance in the piezoelectric material.

2.3.2. Film deposit. The deposition of the piezoelectric films onto the substrate was achieved using an adjustable film applicator, Elcometer 3580 (Elcometer, UK). This device precisely controlled the thickness of the film through micrometric screw adjustments. To perform the deposition, the initial mixture was carefully dispensed upstream of the applicator slide, ensuring an even distribution across the entire width of the slide. Once the mixture was properly positioned, a smooth translational movement was initiated to spread it uniformly, resulting in a film of the expected thickness.

This method ensured consistent and reproducible film deposition, essential for fabricating high-quality piezoelectric sensors. In the context of industrial production, it is worth noting that screen printing could have been a highly advantageous technique due to its scalability, precision, and suitability for mass fabrication processes.

In the final stage, the resulting films were placed in a Memmert (USA) UFE series oven. The first treatment was carried out at 150 °C for 1 h, followed by a second treatment at 285 °C for 1.5 h. These treatments ensured the complete evaporation of solvents and polymerization of the polyimide. Figure 9 illustrates the entire fabrication process.

When the piezoelectric composite was directly deposited onto the part to be monitored, screen printing was used. Substrate preparation involves surface abrasion with 800-grit sandpaper to ensure effective adhesion of the composite. Electrode deposition was also achieved through screen printing, necessitating confirmation of compatibility between the

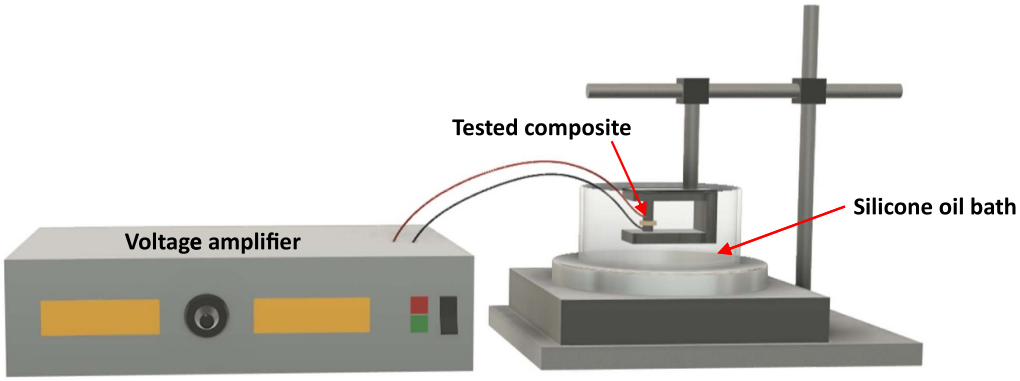

Figure 10. Polarization setup.

conductive ink and the composite (i.e., no solvent-matrix interactions and strong adhesion).

2.3.3. Piezoelectric composite polarization. After curing and cooling the polymer matrix, the upper electrode was deposited using a 208 h sputter coater (Cressington Scientific Instrument, UK). The composite thickness beneath each electrode was then measured to determine the exact voltage required for polarization, ensuring optimal sensor performance.

During polarization, precise electric fields were applied to the specimens (figure 10). To prevent electrical breakdown and ensure uniform temperature, samples, and electrical contacts were submerged in a silicone oil bath, with temperatures adjustable from 50 °C to 180 °C. The electric field was maintained for 30 min. After polarization, samples were cooled under the applied electric field using forced air, preventing depolarization during cooling.

The complete manufacturing process is highly scalable, relying on standard mixing, casting, and curing techniques adaptable to industrial production.

3. Characterization of the permanent printed sensors

We prepared various piezoelectric films to identify the one with the highest piezoelectric coefficient (d_{33}). Parameters available to optimize this coefficient include the matrix choice, the volume fraction of piezoelectric particles within the composite, particle selection, and the polarization temperature and applied electric field amplitude.

3.1. Formulation characterization

A high particle volume fraction (>30 vol.%) is necessary to achieve notable piezoelectric behavior. Initial permittivity measurements (figure 11) revealed that composites with particle loadings up to 40 vol.% did not align with the predictions of the Jayasundere and Smith model (equation (6) [48],),

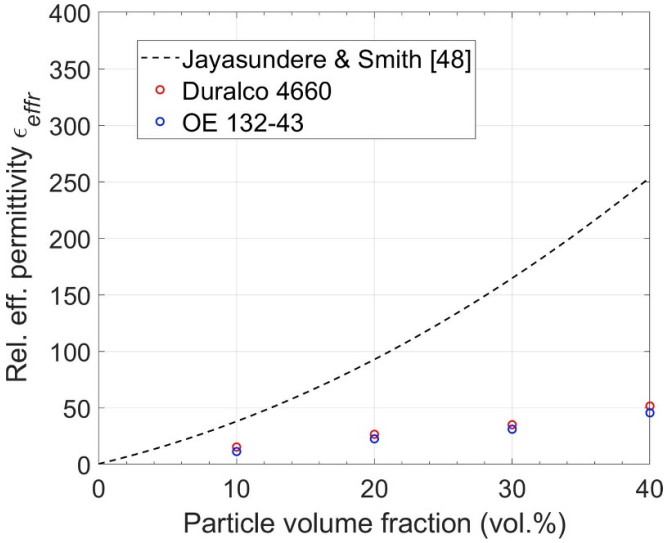

Figure 11. Comparison between Jayasundere and Smith [48] simulation results and experimental measurements obtained for composites elaborated either with Duralco 4660 matrix or with OE132-43 matrix.

indicating non-homogeneity within the composites.

$$\varepsilon_{eff} = \varepsilon_m \cdot \frac{1 + 2\,part\,vol.\% \cdot \frac{\varepsilon_p - \varepsilon_m}{\varepsilon_p + 2\varepsilon_m}}{1 - part\,vol.\% \cdot \frac{\varepsilon_p - \varepsilon_m}{\varepsilon_p + 2\varepsilon_m}} \tag{6}$$

Where ε_{eff} represents the effective permittivity, ε_m denotes the permittivity of the matrix, and ε_p corresponds to the permittivity of the particles. It is worth noting that other models, such as the Maxwell-Garnett model [49], were tested but proved even less successful.

Scanning electron microscope (SEM) analyses of composite cross-sections revealed significant particle sedimentation within the polymer matrix (figure 12). We identified two layers: a sedimented particle layer near the substrate and a pure polymer matrix layer. This sedimentation arises from the high density of PZT particles, low composite viscosity, and high temperatures (120 °C–150 °C) during polymerization or solvent evaporation, allowing particles to settle.

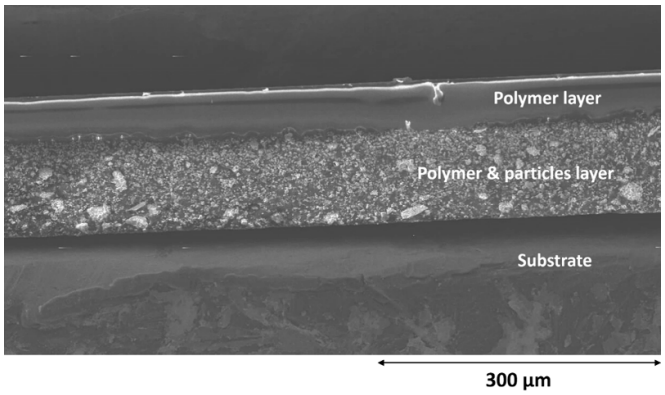

Figure 12. SEM image of a Duralco 4660-based composite filled with 30 vol.% P189 particles.

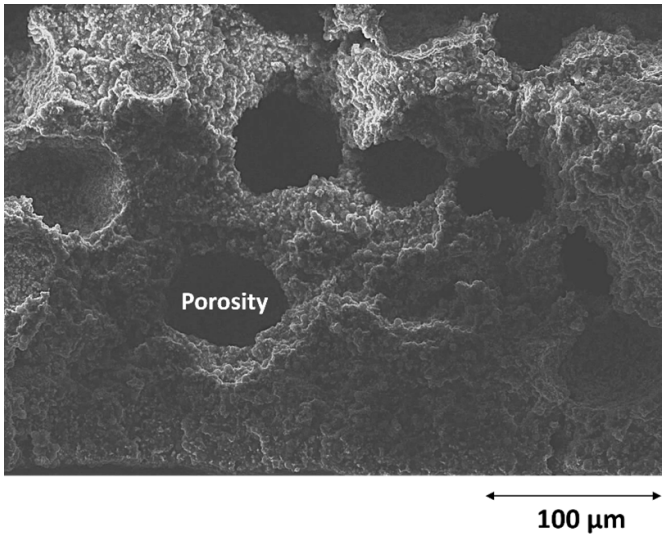

Figure 13. SEM image of an epoxy-based composite filled with 30 vol.% P189 particles.

Polarization of such composites is challenging due to uneven electric field distribution caused by permittivity contrasts between the layers [50]. The electric field concentrates in the polymer layer, limiting polarization in the composite layer. Higher particle loading reduces the polymer layer thickness, promoting a more uniform field and facilitating piezoelectric behavior.

Attempts to remove the polymer surface layer by polishing weakened dielectric properties, introducing defects that caused premature breakdown. Dispersants to modify particle-polymer interactions showed limited success, as sedimentation remained inevitable due to particle density.

The matrix was saturated with particles to prevent settling and counteract sedimentation. Formulation tests determined the maximum feasible loading rate, balancing sufficient fluidity for deposition with adhesion, brittleness, and porosity formation (figure 13). Excessive porosity reduces permittivity and dielectric strength, making polarization unachievable.

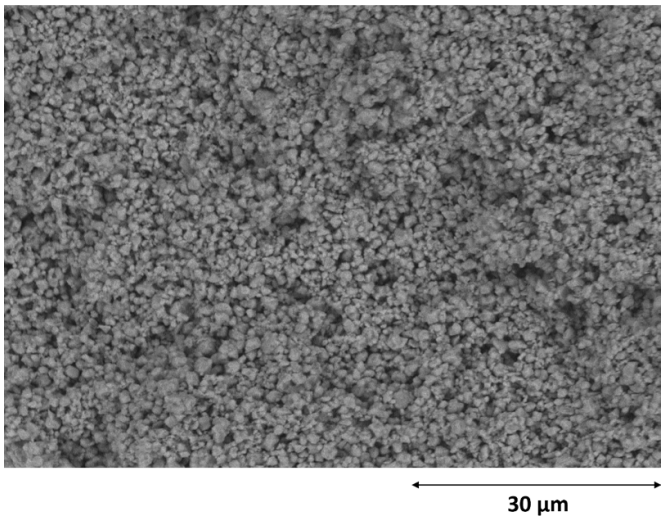

Figure 14. SEM image of a polyimide-based composite filled with 81 vol.% P189 particles.

3.1.1. Epoxy polymer-based case. The maximum loading rate for the Duralco 4460 epoxy matrix is 43 vol.%. Exceeding this threshold causes the mixture to adopt a cement-like consistency, rendering film deposition impractical due to poor substrate adhesion, aggregate formation, and unsuitability for screen printing. The resulting film exhibits high porosity, significantly reducing the composite's dielectric strength, with dielectric breakdown occurring at voltages well below the coercive field of PZT particles, thereby preventing polarization.

3.1.2. Polyimide polymer-based case. EO 132–43, composed of pure polyimide, allows a high particle loading rate of up to 81 vol.% (figure 14). Additionally, the polyimide matrix undergoes significant evaporation during the drying and polymerization phase, enabling a high loading rate while preserving a manageable base mixture for deposition. This fluidity ensures uniformity in the final composite.

At high particle volume percentages, gradual mixing using dispersion methods (e.g. ultrasonic) is essential. After mixing, the viscosity of the resulting mixture was measured at 65 Pa·s with a Physica MCR 301 rheometer (Anton Paar, Austria), falling well within the optimal range for screen printing applications (50–150 Pa·s).

3.2. Polarization characterization

The charge coefficient d33 typically increases with the polarization electric field until saturation in piezoelectric composites. In this study, we applied a bias voltage at 90% of the sample's breakdown voltage to achieve maximum d_{33} while protecting the sample. Breakdown field values were determined using Weibull distributions (figure 7), requiring destructive testing for each composite. For printed composites, leakage current monitoring can estimate breakdown fields, allowing early detection and voltage stabilization to prevent damage.

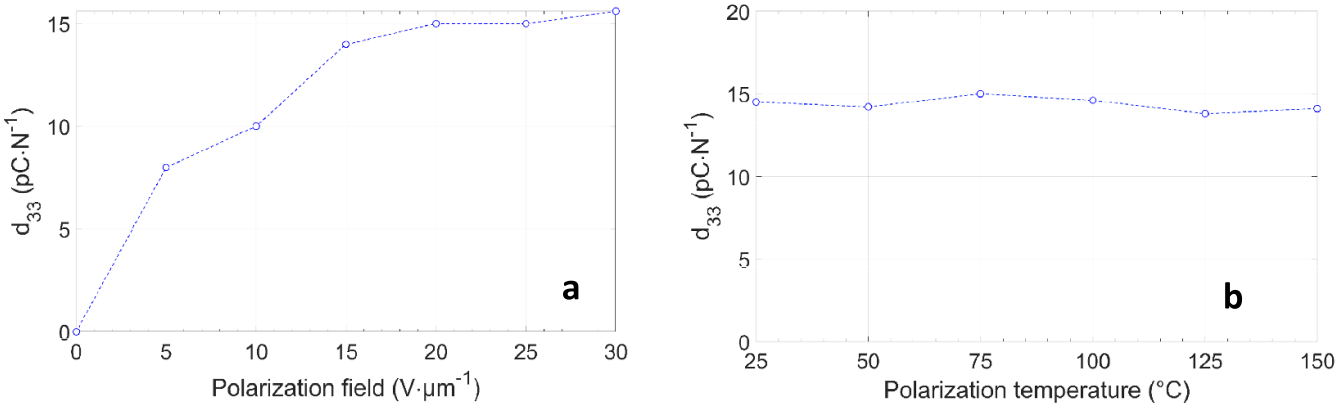

Figure 15. (a) Piezoelectric coefficient d_{33} vs. polarization field for the OE132-43/P189 composite (80 vol.%). (b) Piezoelectric coefficient d_{33} vs. polarization temperature the OE132-43/P189 composite (80 vol.%).

Polarization requires an electric field exceeding the coercive field of the piezoelectric material, approximately 2 kV·mm^{-1} for PZT P189 ceramics [51]. The polymer matrix alters electric field distribution, necessitating a higher polarization field. Incremental electric field tests (figure 15(a)) revealed that the piezoelectric coefficient increases significantly up to 15 V·μm^{-1}, after which it saturates. A 20 V·μm^{-1} bias field is enough to maximize the composite's properties.

Raising polarization temperature can enhance efficiency by increasing polymer matrix permittivity and charge mobility. However, these free charges can lead to an artificially elevated d_{33} measurement immediately after polarization, requiring a relaxation period for charges to stabilize. A high-temperature short circuit dissipates these charges, ensuring accurate measurements. Polarization tests at various temperatures on OE132-43/P189 composites (figure 15(b)) showed consistent d_{33} values, confirming temperature-independent performance for this formulation.

The OE132-43 matrix exhibits minimal permittivity changes at tested temperatures. To induce a significant permittivity increase require polarization above the glass transition temperature (∼250 °C for standard polyimides) [52]. High particle loading further limits polymer influence on dielectric properties. Finally, room temperature polarization was chosen to reduce breakdown risk, enabling higher electric fields with minimal sample damage.

3.3. Dielectric breakdown characterization

Dielectric breakdown tests were conducted on EO 132–43 composites loaded with over 80 vol.% particles and a thickness of 120 μm. The results (figure 16) indicate that achieving a dielectric strength of at least 21 V·μm^{-1} is necessary to attain the maximum piezoelectric coefficient. A polarization range of 18–20 V·μm^{-1} allows for optimized composite performance while minimizing the risk of breakdown. The Weibull distribution (equation (3)) optimized parameters used in figure 16 were $\eta = 33.4$ V·μm^{-1} and $m = 4.8$.

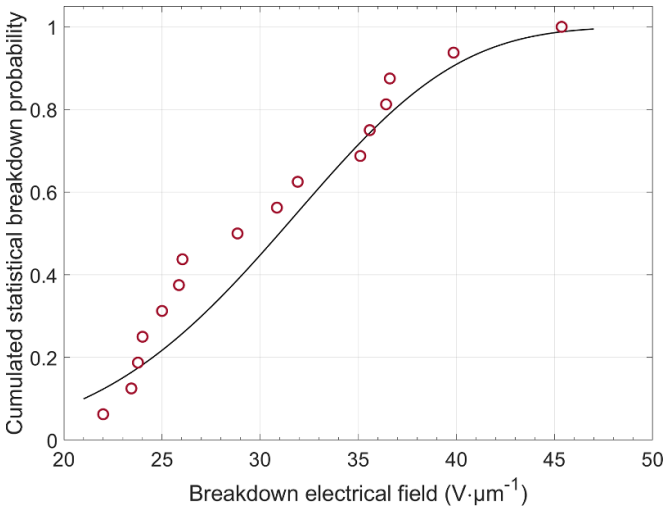

Figure 16. Weibull plot of cumulative breakdown probability for the OE 132–43/P189 (80 vol.%) composite.

4. Experimental results

All experiments were conducted using the UTC 110 system from Eurosonic Ultrasonic Technology (Germany).

4.1. Portable US sensors

We prepared US sensors using the OE 132–43/P189 composite (80 vol.%). The prototypes were deposited onto aluminum metal sheet substrates with a reduced thickness of 100 μm. The manufacturing process employed a silkscreen deposition method, though controlling the deposition thickness posed challenges, requiring precise adjustments for polyimide removal and solvent evaporation. Despite these challenges, we successfully produced sensors with a range of thicknesses, covering a broad frequency spectrum from 1 to 20 MHz, suitable for most targeted applications. Initial tests indicate that the fabricated sensors demonstrate strong measurement capabilities when applied to steel and aluminum components. Figure 17 shows the experimental validation

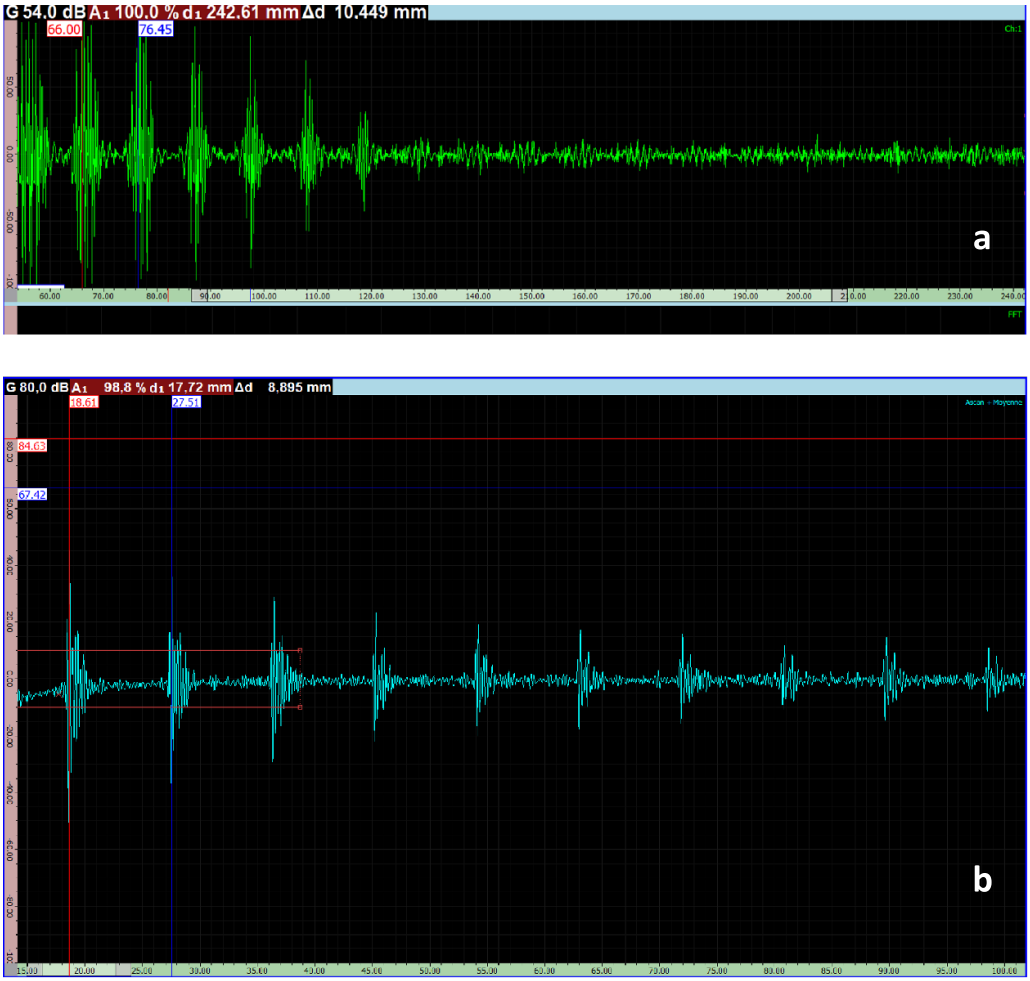

Figure 17. Experimental response of an OE 132–43/P189 (80 vol.%) portable US sensor for thickness evaluation: (a) 10.5 mm thick steel block; (b) 8.9 mm thick aluminum block.

of these capabilities, highlighting the thickness measurement performance of the portable sensor on two distinct materials. In figure 17(a), the ultrasound oscillogram corresponds to a 10.5 mm thick steel block, and in figure 17(b), to an 8.9 mm thick aluminum block. The oscillograms show the ultrasonic wave time-of-flight. We used this signal to evaluate the tested part thickness based on material sound velocity. The device, pre-set with material properties, provided accurate thickness measurements, closely matching actual values. Reflected signals from the back walls of both samples confirm the OE 132–43/P189 sensor's ability for non-destructive thickness evaluation across a wide frequency range. This result demonstrates the sensor's precision and reliability for assessing steel and aluminum components in industrial applications.

4.2. Printed US sensors

US sensors were directly deposited on a 2.5 mm steel test component (figure 18(a)), with the steel acting as the lower electrode and eliminating the need for impedance matching. Results (figure 18(b)) confirmed accurate thickness measurements, demonstrating the feasibility of this approach for direct applications.

However, this method is more constrained than portable sensors printed on polymer or metal foils. Permanent sensors require heating during composite fabrication, necessitating parts that fit an oven for polymerization. The high-voltage polarization step also requires a safety perimeter, limiting direct printing in industrial environments.

The following validation stage involved the 17.8 mm thick steel tube shown in figure 1. We obtained excellent thickness estimations with the printed US sensor (figure 19), confirming the method's viability for industrial-type elements.

Finally, we developed multi-layer sensors consisting of two piezoelectric layers with opposing polarization orientations. Experimental results indicate that these sensors operate within a similar frequency range as single-layer sensors with a thickness equivalent to the combined thickness of the multi-layer design. Notably, multi-layer sensors produce increased acoustic pressure (higher echo intensity), making them a valuable alternative by enabling lower voltage operation while achieving comparable performance and even improved penetration, allowing for the measurement of thicker components.

Figure 18. (a) Picture of a printed US permanent sensor (b) experimental response of an OE 132–43/P189 (80 vol.%) permanent US sensor for the thickness evaluation of a 2.5 mm thick steel block.

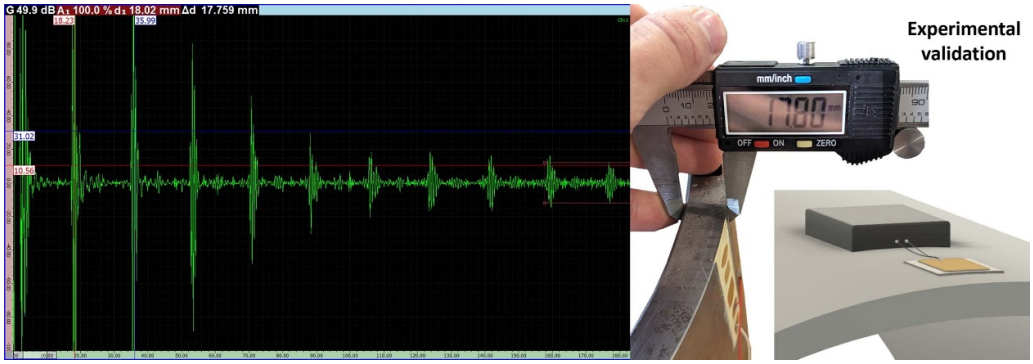

Figure 19. Validation of the printed US sensor on a 17.80 mm thick steel in an industrial context.

5. Conclusions

This study developed an innovative ultrasound (US) sensor technology for structural health monitoring (SHM) by directly printing sensors onto critical components. We achieved improved performances with a piezoelectric composite based on an OE 132–43 polyimide matrix combined with P189 NAVY III-type piezoelectric ceramic particles at 80 vol.%. The active composite enabled reliable results across a broad frequency spectrum (1–20 MHz) and diverse substrates such as aluminum and steel.

Compared to high-performance materials like PMN-PT or PZT-based ceramics, the printed composites sacrifice some sensitivity and stability in exchange for distinct advantages, including cost-effectiveness, scalability, and the ability to be directly printed onto components with complex geometries.

Despite certain constraints, such as the need for oven polymerization and adherence to high-voltage safety protocols, the technology's ability to deliver stable, high-resolution measurements makes it a promising candidate for long-term monitoring applications. Additionally, the fabrication of multi-layer sensors further enhanced echo intensity at lower operating voltages, supporting applications on thicker structural elements.

Future research will expand upon this work with the following focal points:

_ Experimental Validation Across Substrates: Verifying the resonance frequencies of the developed sensors across alternative substrates (carbon fibers, etc.).
_ Optimization of Acoustic Impedance: Enhancing the signal-to-noise ratio by optimizing the acoustic impedance of the piezoelectric composite sensors (tailoring particle-matrix ratios or integrating matching layers, etc.) [47].
_ Environmental Robustness Testing: Experimentally assess the sensor's performance under alternative environmental conditions (temperature, humidity, and mechanical stress).
_ Long term durability: Controlling the printed sensor's performances over extended periods of time.

Data availability statement

All data that support the findings of this study are included within the article (and any supplementary files).

Funding

This work was supported by the French Direction Générale de l'Armement (DGA) as part of the RAPID DGA project CMICA vf-28508.

ORCID iDs

Guilhem Rival https://orcid.org/0000-0002-5904-9007
Arnaud Pelletier https://orcid.org/0009-0009-6104-1790
Benjamin Ducharne https://orcid.org/0000-0002-2046-211X

References

[1] Balageas D, Fritzen C P and Güemes A (eds) 2010 *Structural Health Monitoring* vol 90 (Wiley)

[2] Farrar C R and Worden K 2012 *Structural Health Monitoring: A Machine Learning Perspective* (Wiley)

[3] Giurgiutiu V 2015 Structural health monitoring of aerospace composites (Academic)

[4] Wright R F, Lu P, Devkota J, Lu F, Ziomek-Moroz M and Ohodnicki P R Jr 2019 Corrosion sensors for structural health monitoring of oil and natural gas infrastructure: a review *Sensors* **19** 3964

[5] Agdas D, Rice J A, Martinez J R and Lasa I R 2016 Comparison of visual inspection and structural health monitoring as bridge condition assessment methods *J. Perform. Constr. Facil.* **30** 04015049

[6] Goyal D and Pabla B S 2016 The vibration monitoring methods and signal processing techniques for structural health monitoring: a review *Arch. Comput. Methods Eng.* **23** 585–94

[7] Montalvao D, Maia N M M and Ribeiro A M R 2006 A review of vibration-based structural health monitoring with special emphasis on composite materials *Shock Vib. Dig.* **38** 295–324

[8] Sodano H A 2007 Development of an automated eddy current structural health monitoring technique with an extended sensing region for corrosion detection *Struct. Health Monit.* **6** 111–9

[9] Brun E, Cottinet P J, Pelletier A and Ducharne B 2023 Printed Eddy current testing sensors: toward structural health monitoring applications *Sensors* **23** 8345

[10] Mutlib N K, Baharom S B, El-Shafie A and Nuawi M Z 2016 Ultrasonic health monitoring in structural engineering: buildings and bridges *Struct. Control Health Monit.* **23** 409–22

[11] Michaels J E 2008 Ultrasonic structural health monitoring: strategies, issues, and progress *Smart Sensor Phenomena, Technology, Networks, and Systems 2008* vol 6933 (SPIE) pp 267–78

[12] Mustapha S, Lu Y, Ng C T and Malinowski P 2021 Sensor networks for structures health monitoring: placement, implementations, and challenges—a review *Vibration* **4** 551–85

[13] Nagayama T and Spencer B F Jr 2007 Structural health monitoring using smart sensors *Newmark Structural Engineering Laboratory Report Series* 001

[14] Yu L and Giurgiutiu V 2007 *In-situ* optimized PWAS phased arrays for Lamb wave structural health monitoring *J. Mech. Mater. Struct.* **2** 459–87

[15] Huan Q, Chen M, Su Z and Li F 2019 A high-resolution structural health monitoring system based on SH wave piezoelectric transducers phased array *Ultrasonics* **97** 29–37

[16] Ali S H, Khan T M R, Abdullah M and Zaid M 2021 Wireless sensor network–based structural health monitoring of bridges using advanced signal processing techniques *J. Test. Eval.* **49** 1266–83

[17] Yang Y, Chen T, Lin W, Jing M and Xu W 2024 Research progress on calibration of bridge structural health monitoring sensing system *Adv. Bridge Eng.* **5** 32

[18] Catbas N, Gokce H B and Frangopol D M 2013 Predictive analysis by incorporating uncertainty through a family of models calibrated with structural health-monitoring data *J. Eng. Mech.* **139** 712–23

[19] Zonta D, Wu H, Pozzi M, Zanon P, Ceriotti M, Mottola L, Picco G P, Murphy A L, Guna S and Corra M 2010 Wireless sensor networks for permanent health monitoring of historic buildings *Smart Struct. Syst.* **6** 595–618

[20] Gonzalez Rodriguez D, Garcia J, Ducharne B, Voyles R, Nawrocki R A and Newell B 2020 3D printing of flexible sensing actuators *Smart Materials, Adaptive Structures and Intelligent Systems* vol 84027 (American Society of Mechanical Engineers) p V001T01A004

[21] Mamer T, Garcia J, Leon-Salas W D, Voyles R, Nawrocki R A, Yokota T, Someya T, Ducharne B and Newell B 2020 Production of 3D printed flexible strain sensors *Smart Materials, Adaptive Structures and Intelligent Systems* vol 84027 (American Society of Mechanical Engineers) p V001T01A003

[22] Akdogan E K, Allahverdi M and Safari A 2005 Piezoelectric composites for sensor and actuator applications *IEEE Trans. Ultrason. Ferroelectr. Freq. Control* **52** 746–75

[23] Kabakov P, Kim T, Cheng Z, Jiang X and Zhang S 2023 The versatility of piezoelectric composites *Annu. Rev. Mater. Res.* **53** 165–93

[24] Newnham R E, Bowen L J, Klicker K A and Cross L E 1980 Composite piezoelectric transducers *Mater. Des.* **2** 93–106

[25] Guyomar D, Ducharne B and Sebald G 2011 High nonlinearities in Langevin transducer: a comprehensive model *Ultrasonics* **51** 1006–13

[26] Guyomar D, Ducharne B and Sebald G 2010 High frequency bandwidth polarization and strain control using a fractional derivative inverse model *Smart Mater. Struct.* **19** 045010

[27] Dumont-Fillon J (ed) 1996 *Contrôle non destructif (CND)* (Techniques Ingénieur)

[28] Sundaram S, Sampathkumar P, Gowdhaman P and Annamalai V 2014 Dielectric and piezoelectric properties of various ferroelectric ceramic-polymer composites *J. Environ. Nanotechnol.* **3** 27–31

[29] Ibrahim M E 2021 Ultrasonic inspection of hybrid polymer matrix composites *Compos. Sci. Technol.* **208** 108755

[30] Kim K Y, Park K H, Park H C, Goo N S and Yoon K J 2005 Performance evaluation of lightweight piezo-composite actuators *Sens. Actuators* A **120** 123–9

[31] Gohari S, Sharifi S, Abadi R, Izadifar M, Burvill C and Vrcelj Z 2018 A quadratic piezoelectric multi-layer shell element for FE analysis of smart laminated composite plates induced by MFC actuators *Smart Mater. Struct.* **27** 095004

[32] Jha A K and Prasad K 2010 Ferroelectric $BaTiO_3$ nanoparticles: biosynthesis and characterization *Colloids Surf.* B **75** 330–4

[33] Liu C, Zou B, Rondinone A J and Zhang Z J 2001 Sol− gel synthesis of free-standing ferroelectric lead zirconate titanate nanoparticles *J. Am. Chem. Soc.* **123** 4344–5

[34] Uchino K (ed) 2017 *Advanced Piezoelectric Materials: Science and Technology* (Woodhead Publishing)

[35] Kwon K O and Yu I J 2005 Globally harmonized system of classification and labelling of chemicals (GHS) *In Proc. Korea Institute of Fire Science and Engineering Conf.* pp 21–34

[36] Blitz J and Simpson G 1995 *Ultrasonic Methods of Non-destructive Testing* vol 2 (Springer)

[37] Aurelle N, Roche D, Richard C and Gonnard P 1994 Sample aspect ratio influence on the shear coefficients measurements of a piezoelectric bar *Proc. 1994 IEEE Int. Symp. on Applications of Ferroelectrics* (IEEE) pp 162–5

[38] Albareda A, Gonnard P, Perrin V, Briot R and Guyomar D 2000 Characterization of the mechanical nonlinear behavior of piezoelectric ceramics *IEEE Trans. Ultrason. Ferroelectr. Freq. Control* **47** 844–53

[39] Rjafallah A, Hajjaji A, Belhora F, El Ballouti A, Touhtouh S, Guyomar D and Boughaleb Y 2020 PZT ceramic particles/polyurethane composites formalism for mechanical energy harvesting *Eur. Phys. J. Appl. Phys.* **89** 30901

[40] Kurita H, Wang Z, Nagaoka H and Narita F 2020 Fabrication and mechanical properties of carbon-fiber-reinforced

polymer composites with lead-free piezoelectric nanoparticles *Sens. Mater.* **32** 2453–62
[41] Zhang F, Saleh E, Vaithilingam J, Li Y, Tuck C J, Hague R J, Wildman R D and He Y 2019 Reactive material jetting of polyimide insulators for complex circuit board design *Addit. Manuf.* **25** 477–84
[42] Zhou P *et al* 2021 Thermally stable, adhesively strong graphene/polyimide films for inkjet printing ultrasound sensors *Carbon* **184** 64–71
[43] Pedroli F, Flocchini A, Marrani A, Le M Q, Sanseau O, Cottinet P J and Capsal J F 2020 Boosted energy-storage efficiency by controlling conduction loss of multilayered polymeric capacitors *Mater. Des.* **192** 108712
[44] Pedroli F 2020 Dielectric strength and leakage current: from synthesis to processing optimization *Doctoral Dissertation* Institut National des Sciences Appliquées de Lyon
[45] Liu W, Zhu C and Wu D 2021 Flexible piezoelectric micro ultrasonic transducer array integrated on various flexible substrates *Sens. Actuators* A **317** 112476
[46] Henri V, Dantras E, Lacabanne C, Koliatene F and Trebosc C 2021 Ageing of polyimide under thermal stress: relaxational effects and charge transport *Polym. Degrad. Stab.* **186** 109524
[47] Rathod V T 2020 A review of acoustic impedance matching techniques for piezoelectric sensors and transducers *Sensors* **20** 4051
[48] Jayasundere N and Smith B V 1993 Dielectric constant for binary piezoelectric 0-3 composites *J. Appl. Phys.* **73** 2462–6
[49] Mallet P, Guérin C A and Sentenac A 2005 Maxwell-garnett mixing rule in the presence of multiple scattering: derivation and accuracy *Phys. Rev.* B **72** 014205
[50] Venkatesh M S and Raghavan G S V 2005 An overview of dielectric properties measuring techniques *Can. Biosyst. Eng.* **47** 15–30
[51] Waechter D F, Prasad S E, Blacow R G and Yan B 2005 Internally biased PZT materials for high-power sonar transducers *Proc. 11th CF/DRDC Int. Meeting on Naval Applications of Materials Technology* (*Dartmouth, Nova Scotia, Canada*, *7th–9th June*)
[52] Liaw D J, Hsu P N, Chen W H and Lin S L 2002 High glass transitions of new polyamides, polyimides, and poly (amide− imide) s containing a triphenylamine group: synthesis and characterization *Macromolecules* **35** 4669–76